AD-A156 574 CHARACTERIZATION OF MECHANICAL DAMAGE MECHANISMS IN CERAMIC COMPOSITE MATERIALS(U) SOUTHWEST RESEARCH INST SAN ANTONIO TX J LANKFORD JUN 85 N00014-84-C-0123 1/1

UNCLASSIFIED F/G 11/4 NL

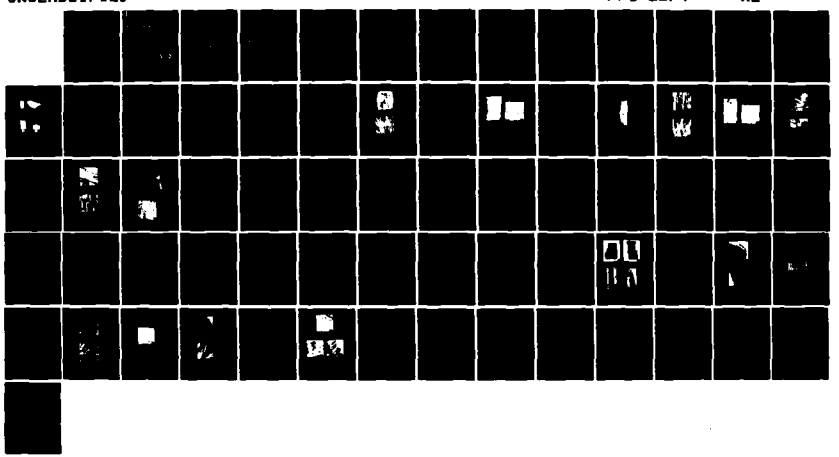

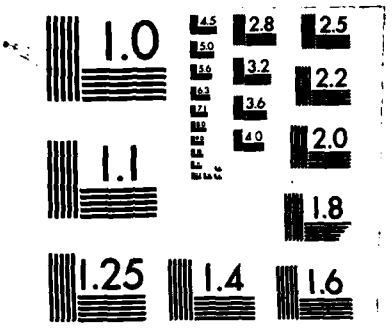

MICROCOPY RESOLUTION TEST CHART
NATIONAL BUREAU OF STANDARDS-1963-A

SwRI-8124/2

12

CHARACTERIZATION OF MECHANICAL DAMAGE MECHANISMS IN CERAMIC COMPOSITE MATERIALS

By
James Lankford, Jr.

TECHNICAL REPORT

ONR CONTRACT NO. N00014-84-C-0213
ONR Contract Authority NR 032-553/11-10-83(430)
SwRI-8124

For
Office of Naval Research
Arlington, VA 22217

By
Southwest Research Institute
San Antonio, Texas

June 1985

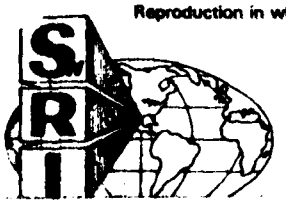

SOUTHWEST RESEARCH INSTITUTE
SAN ANTONIO HOUSTON

UNCLASSIFIED

SECURITY CLASSIFICATION OF THIS PAGE (When Data Entered)

REPORT DOCUMENTATION PAGE	READ INSTRUCTIONS BEFORE COMPLETING FORM
1. REPORT NUMBER	2. GOVT ACCESSION NO. AD-A156 571 / 3. RECIPIENT'S CATALOG NUMBER
4. TITLE (and Subtitle) Characterization of Mechanical Damage Mechanisms in Ceramic Composite Materials	5. TYPE OF REPORT & PERIOD COVERED Interim Technical Report 24 May 1984 - 23 May 1985
	6. PERFORMING ORG. REPORT NUMBER 06-8124
7. AUTHOR(s) James Lankford	8. CONTRACT OR GRANT NUMBER(s) N00014-84-C-0123
9. PERFORMING ORGANIZATION NAME AND ADDRESS Southwest Research Institute 6220 Culebra Road, P.O. Drawer 28510 San Antonio, TX 78284	10. PROGRAM ELEMENT, PROJECT, TASK AREA & WORK UNIT NUMBERS NR 032-553/11-10-83(430)
11. CONTROLLING OFFICE NAME AND ADDRESS Office of Naval Research 800 North Quincy Arlington, VA 22217	12. REPORT DATE June 1985
	13. NUMBER OF PAGES
14. MONITORING AGENCY NAME & ADDRESS(if different from Controlling Office)	15. SECURITY CLASS. (of this report) Unclassified
	15a. DECLASSIFICATION/ DOWNGRADING SCHEDULE

16. DISTRIBUTION STATEMENT (of this Report)

This document has been approved for public release and sale; its distribution is unlimited.

17. DISTRIBUTION STATEMENT (of the abstract entered in Block 20, if different from Report)

18. SUPPLEMENTARY NOTES

19. KEY WORDS (Continue on reverse side if necessary and identify by block number)

Compressive Strength
Partially Stabilized Zirconia
Temperature Effects
Composite Materials
Fracture Mechanisms
Ceramics
Plastic Flow

20. ABSTRACT (Continue on reverse side if necessary and identify by block number)

This report summarizes research performed on two distinctly different ceramic composite materials. One was SiC-fiber reinforced LAS glass, while the other was an yttrium partially-stabilized, tetragonal-cubic phase zirconia.

Silicon carbide fiber reinforced glass-ceramic matrix composite material has been tested in compression over a wide range in temperature. Both unidirectionally and multiaxially reinforced composites were tested. Compressive

DD FORM 1473 EDITION OF 1 NOV 65 IS OBSOLETE

SECURITY CLASSIFICATION OF THIS PAGE (When Data Entered)

strength was measured, and pre-failure damage mechanisms characterized using acoustic emission and optical and scanning electron microscopy. Results are contrasted with corresponding tensile failure modes, and interpreted in terms of matrix microfracture, fiber kinking, and fiber orientation.

Deformation and failure mechanisms are characterized for fully and partially yttria-stabilized single crystals tested in compression from 23C to 1150C. It is found that both types of material exhibit extensive plastic flow over most of this temperature range, producing rapid decreases in strength with increasing temperature. Tetragonal to monoclinic transformation-induced plasticity is not observed; rather, plastic flow is related solely to dislocation activity. Evidence is found for apparent cubic to rhombohedral transformation during polishing, and reverse rhombohedral to cubic transformation during imposed compressive stress.

Additional keywords: fracture (mechanics); Naval research.

FOREWORD

This report describes recent work carried out under an experimental program aimed at characterizing damage mechanisms and compressive failure in ceramic-matrix composite materials. The report consists of two papers, each to be published in, or having been submitted to, the journal noted on its title page.

TABLE OF CONTENTS

LIST OF ILLUSTRATIONS

LIST OF ILLUSTRATIONS (CONTINUED)

International Conference on Composite Materials (in press)

I.
COMPRESSIVE STRENGTH AND DAMAGE MECHANISMS IN A SiC-FIBER REINFORCED GLASS-CERAMIC MATRIX COMPOSITE

James Lankford
Department of Materials Sciences
Southwest Research Institute
San Antonio, Texas 78284 USA

ABSTRACT

Silicon carbide fiber reinforced glass-ceramic matrix composite material has been tested in compression over a wide range in temperature. Both unidirectionally and multiaxially reinforced composites were tested. Compressive strength was measured, and pre-failure damage mechanisms characterized using acoustic emission and optical and scanning electron microscopy. Results are contrasted with corresponding tensile failure modes, and interpreted in terms of matrix microfracture, fiber kinking, and fiber orientation.

The support of the Office of Naval Research under Contract Number N00014-84-C-0213 is gratefully acknowledged.

INTRODUCTION

An interesting and technologically promising class of composite materials, based on a lithium aluminosilicate (LAS) glass-ceramic matrix reinforced by continuous SiC fibers, has recently been developed. Most of the mechanical property characterization of these materials has been fairly gross in scale (1), so that failure micromechanisms have not been established. However, material characterization, especially the matrix and matrix-fiber interface chemistry, has received extensive study, and is quite well understood (2). The purpose of this paper is to report the initial results of a study aimed at characterizing the initiation and development of damage during compressive loading of these composites.

Knowledge regarding compressive failure is important for composites, aside from the obvious fact that they may experience compression directly. In particular, flexural failure often initiates on the compressive rather than the tensile side of the specimen (3). This mode of fracture already has been observed for certain SiC reinforced LAS variants tested in 4-point bending (1). Finally, compressive loading is stable; since specimens can absorb an extensive volume of relatively homogeneous damage before finally failing, damage characterization is simplified.

Theoretical analysis of composite failure under compressive loading is not well developed at this time, and is limited to unidirectional fiber layups (3,4). Piggott has considered the effects of such factors as fiber strength, fiber linearity, and matrix-fiber adhesion (3), while Evans and Adler have analyzed the mechanics of failure due to kink development (4). The evolution of these theories to more complex composite microstructures and layups requires guidance in the form of experimental verification of the relevant damage mechanisms.

Extensive work by Prewo (1) has concerned itself with the strength and macroscopic fracture appearance of several matrix variants and layup configurations of SiC reinforced LAS composites tested in flexure, tension, and compression (1) over a wide temperature range. However, only the earliest LAS variant (LAS-I) was tested in compression. This work is complemented by the present study, in which compressive damage micromechanisms in the second generation LAS composite (LAS-II) are related to temperature, composite microstructure, and stress orientation.

EXPERIMENTAL APPROACH

Materials

The materials used in the investigation were SiC-LAS-II panels* provided by United Technologies Research Center through the Office of Naval Research. As-received panels were 10 cm x 10 cm x 0.625 cm, and were in the ceramed condition. The LAS-II material has been extensively characterized by Brennan (2); it differs from LAS-I by the addition of 5 wt.% Nb_2O_5, which enhances high temperature oxidation resistance by forming an NbC oxidation barrier layer on the SiC fibers.

Panels were laid up in two conditions, i.e., unidirectional (0°), in which all of the fibers were oriented more-or-less parallel to one another, and crossplied (0/90), in which unidirectional sheets were crossplied at 90° upon one another. The latter microstructure is shown schematically in Figure 1. Both layups contained approximately 46 vol % fiber, and had an as-ceramed porosity of about 1 vol %.

---

*Panel 2391, (0°) layup.

Panel 2393, (0/90) layup.

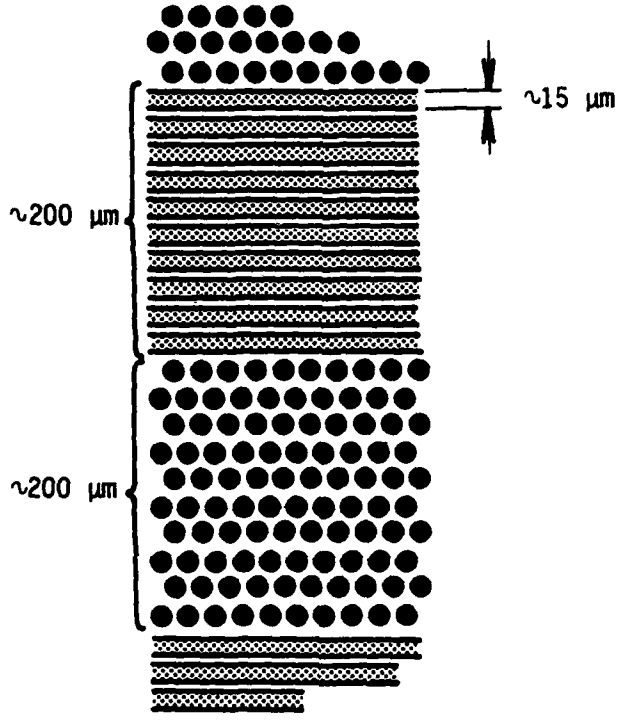

Figure 1. Dimensions and orientations of crossply bundles and fibers.

Procedures

Cylindrical specimens* 1.2 cm long x 0.6 cm in diameter were machined from the panels; their ends were ground parallel to within 2 μm. The compression axis was parallel to the fibers for the 0° specimens, while for the 0/90 material, the load axis was oriented parallel to the 0° direction for one set of specimens, and at 45° to the 0° and 90° fiber bundles for the other set (45/45).

Specimens were tested in air at a strain rate of $1x10^{-4}s^{-1}$, and at temperatures of 23C and 810C (5). In order to prevent brooming (Figure 2a), small rings were honed to just fit, via slight pressure, over the ends of the specimen. Because of the inside taper of the rings, contact occurred only over the last 1.2 mm of each end. This procedure successfully confined failure to the center section of each specimen (Figure 2b).

Yielding was defined by deviation of crosshead displacement from linearity. As a further, more sensitive measure of the onset of damage, acoustic emission (AE) was employed to detect microfracture. The AE setup (6) was activated by a transducer attached to the alumina loading platens (5), outside the hot zone of the furnace.

Following the attainment of ultimate strength, tests were quickly stopped, and each specimen was unloaded as an intact body. Using a slow-speed diamond saw, various sections were then made relative to the fiber layup directions, and the internal damage thereby revealed was characterized by means of optical and scanning electron microscopy.

---

*This specimen design contrasts with that of Prewo for compression testing of LAS-I. The latter specimens were flat dogbones, with gage sections 2.7 cm long x 1.25 cm wide x 0.625 cm thick.

(a) Brooming of unconstrained 0° specimen.

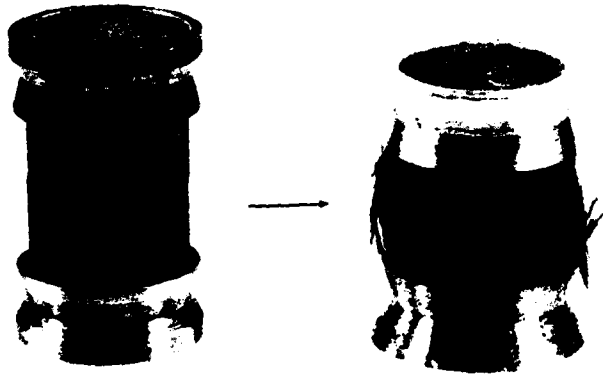

(b) Barreling of constrained 0° specimen.

Figure 2. Effect of end constraint upon compressive failure.

RESULTS

Strength

The effects of temperature and fiber orientation upon compressive strength (σ_C), yield strength (σ_y), and the threshold stress level for acoustic emission (σ_{AE}) are shown in Figure 3. In most cases, failure was preceded by "plastic" yielding, which in turn was preceded by acoustic emission. Exceptions were the 810C tests of the 0/90 and 45/45 layups, in which cases $\sigma_{AE} = \sigma_C$, and the load-deflection curve was linear to failure. The 0° orientation was roughly 3 times as strong as the 0/90, and was more than 500% stronger than the 45/45. In the latter case, the AE response indicated that some form of damage was incurred at stresses of little more than 50 MPa.

In Figure 4, the compressive behavior of LAS-I and LAS-II matrices are compared. It is clear that σ_C for the 0/90 and 45/45 layups is essentially identical for both matrices, while for 0° layups, LAS-II is much stronger.

Finally, the compressive behavior of LAS-II is compared with flexural and tensile strengths in air and Ar (Figure 5). Compressive strength in air and 4-point bend strength in Ar follow essentially the same relationship. Above 600C, 4-point flexural strength in air drops precipitously to that for pure tension, which is low for all temperatures.

Interpretation of these results requires knowledge of the damage states corresponding to each combination of temperature, stress level, environment, composite microstructure, and orientation. Current understanding of these damage mechanisms is outlined in the next section.

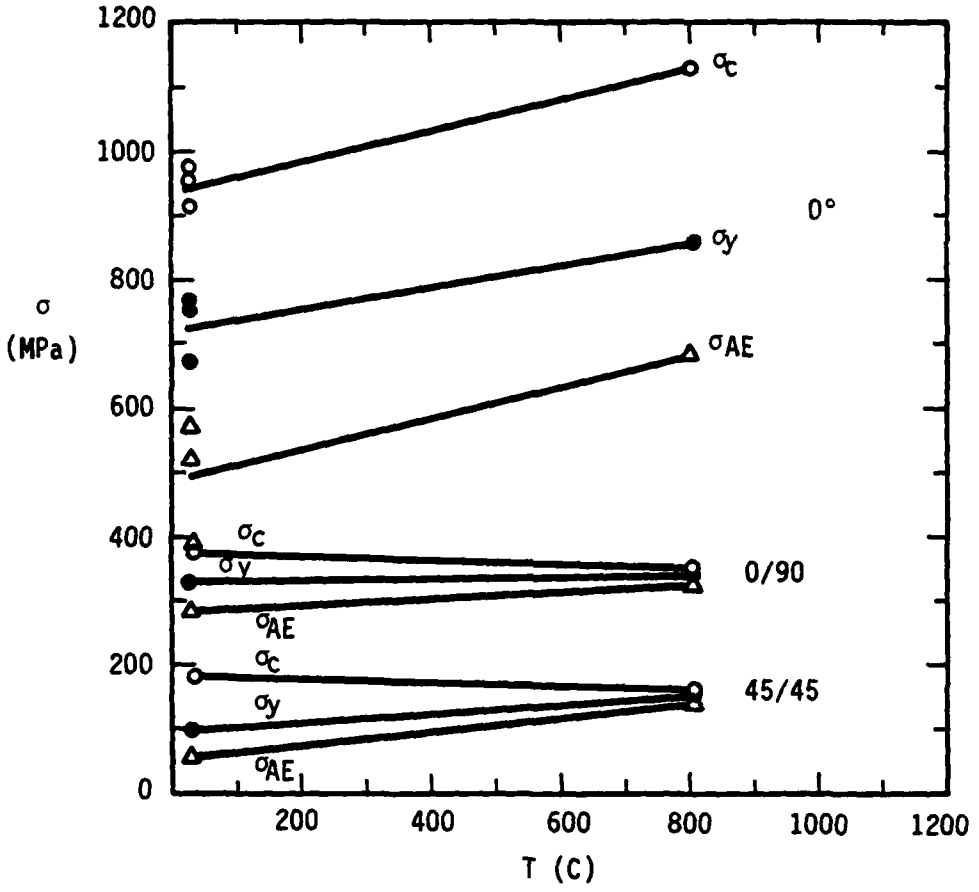

Figure 3. Effect of fiber orientation and temperature on compressive strength, yield strength, and acoustic emission threshold stress level for LAS-II.

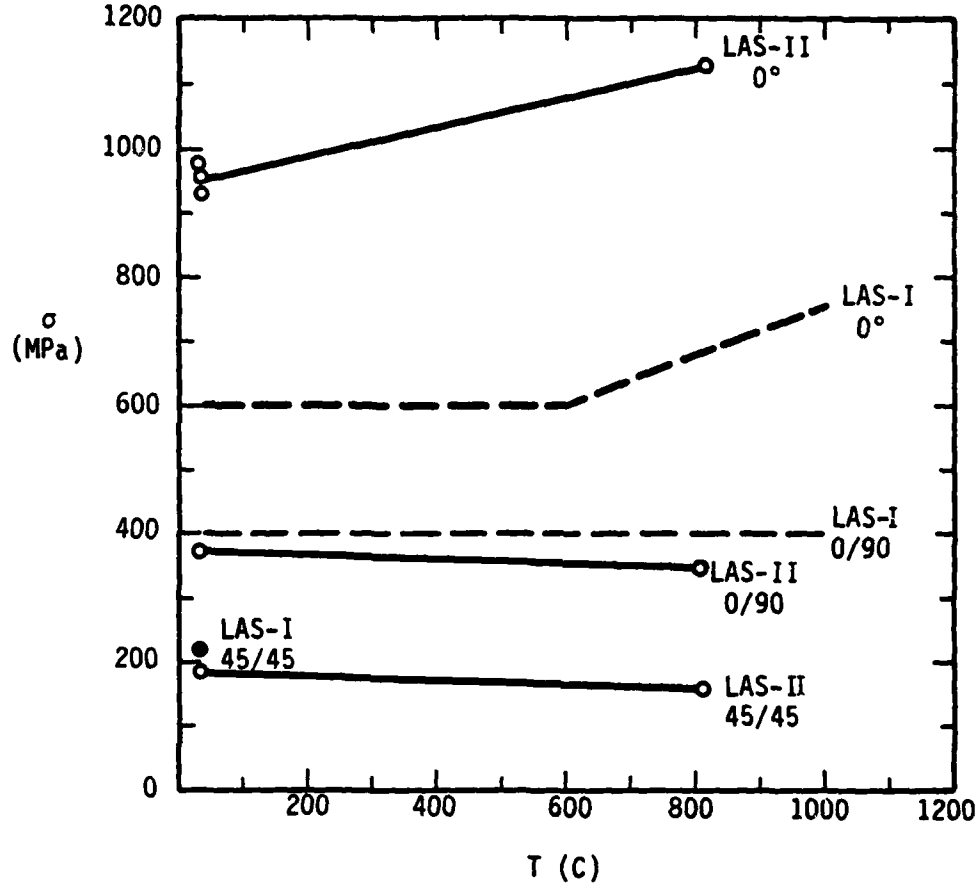

Figure 4. Effect of fiber orientation and temperature upon compressive strength for LAS-I and LAS-II.

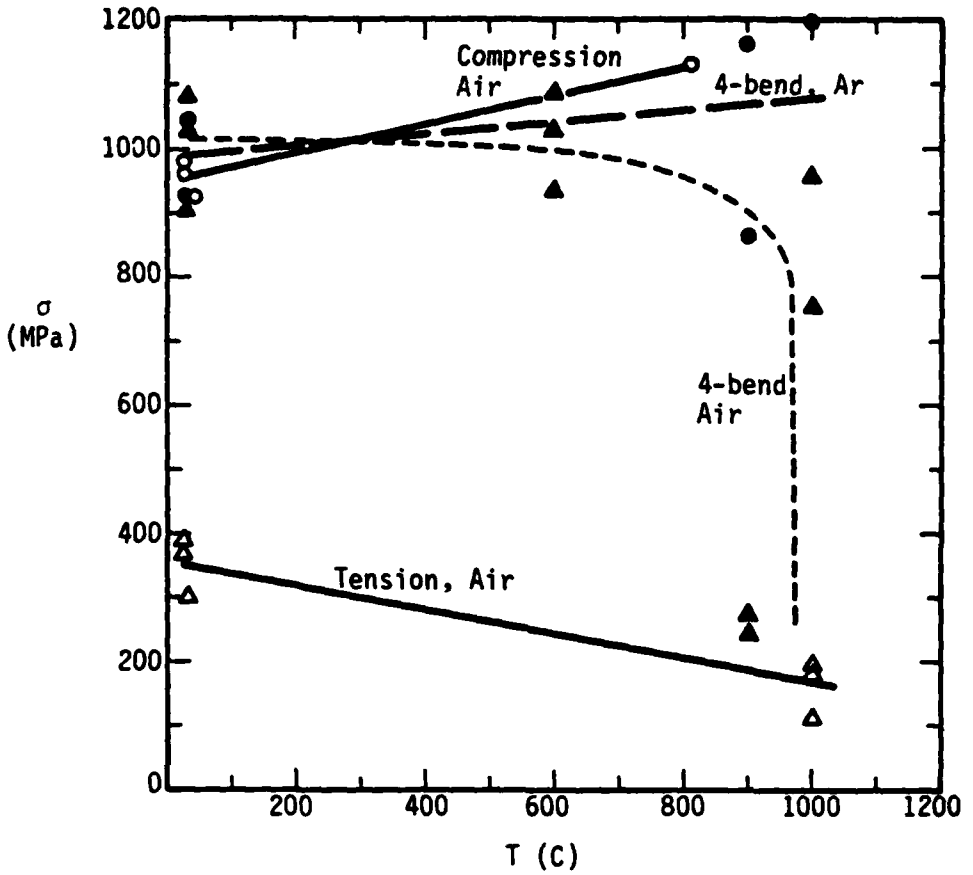

Figure 5. Effect of loading mode, environment, and temperature upon strength for LAS-II.

Failure Mechanisms

Since basically similar damage modes were observed at 23C and 810C, photomicrographs in this section are limited to 23C specimens.

0° Orientation. The 0° layup was observed to fail (Figure 6a) by an isotropic buckling process. Although the V-shaped regions to either side of the specimen constitute macroscopic kinks, most of the fibers contained within the kink regions are merely curved, not broken, and essentially accommodate the buckling.

Within the central void regions which have formed (Figure 6b), it is interesting that individual fibers are frequently devoid of surrounding matrix material. No such voids are present in the elastically deformed regions near the specimen ends, so they cannot be ascribed, except in a secondary sense, to the sectioning process. In particular, the creation of the cut surface apparently allowed the release of compressively damaged matrix material.

0/90 Orientation. Sections through 0/90 layups were made both within the plane of the fiber sheets (in-plane), and normal to those planes (out-of-plane). Figure 7 indicates schematically the appearances of in-plane and out-of-plane kinks for each of these sections, respectively. It will be recognized that kinks normal to the chosen plane of view (e.g., out-of-plane kinks viewed in an in-plane section) will resemble an array of ellipses. Figure 8 shows an in-plane 0/90 section, in which an out-of-plane kink band traverses the entire specimen width. In this case, the kink band, the right hand portion of which is shown in Figure 8b, represents a much more localized deformation event than the macroscopic shape change associated with the 0° specimen. In this view, the specimen sides

(a) Macroscopic view of buckled specimen; kinked regions consist mainly of unbroken fibers.

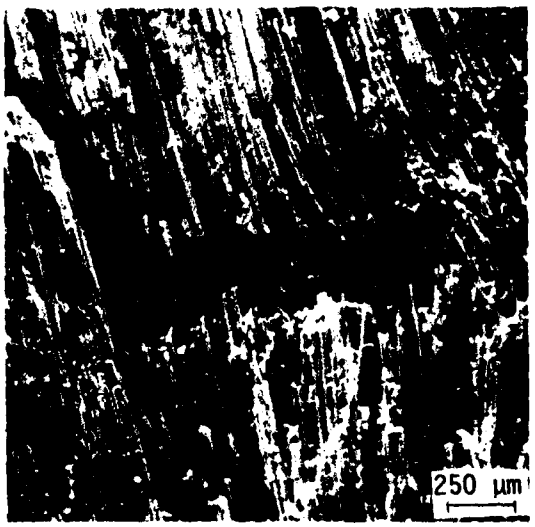

(b) Void near center section; individual fibers devoid of surrounding matrix.

Figure 6. Failure of 0° specimens.

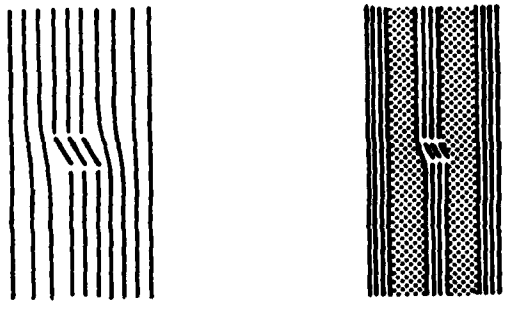

(a) In-plane kink, in-plane section.

(b) Out-of-plane kink, out-of-plane section.

Figure 7. Kink configurations.

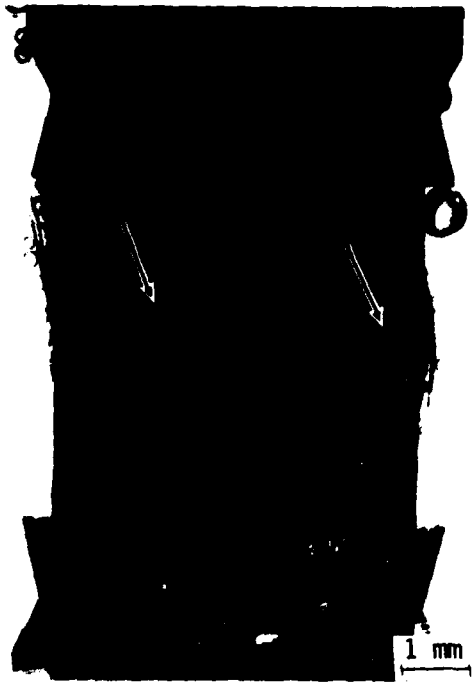

(a) In-plane view of out-of-plane kink traversing specimen gage section (arrow).

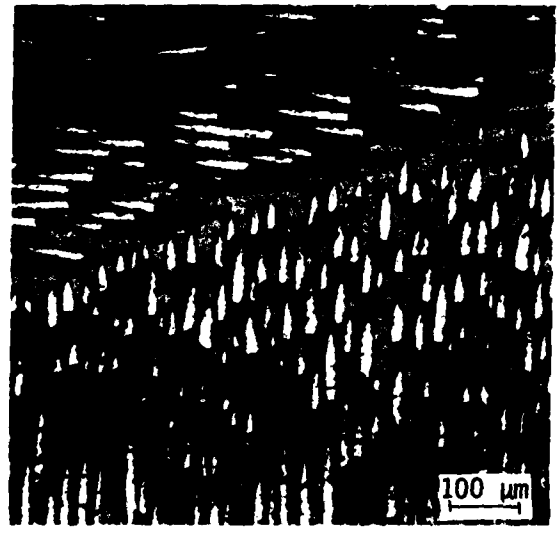

(b) Out-of-plane kink band; note ellipsoidal shape of sectioned fibers.

Figure 8. Macroscopic view of 0/90 specimen.

are still reasonably straight, except for a few fibers which have broken out near the ends of the kink band.

Viewed in an out-of-plane section, however, a series of out-of-plane kinks can be seen (Figure 9) to produce a bulge in the gage section. Recalling Figure 8a, it is clear that the specimen gage section is no longer symmetrical. The kinks which produce the out-of-plane bulge are shown in greater detail in Figure 10a, where it can be seen that they are accompanied by delamination and void formation within the plies oriented at 90° to the compression axis. Intact 90° plies also suffer microfracture within the plane normal to the load axis near intense kink bands (arrows).

Inspection of intense kinks (Figure 10b) shows that such regions are not continuous like the macroscopic 0° kinks, but instead are made up of broken, fairly straight segments. The nearby voids in the 90° plies are not caused by fracture of the 90° fibers; in every instance observed, the void "crack" passes totally within the LAS matrix, and around the fibers.

45/45 Orientation. In-plane sectioning of 45/45 specimens (Figure 11a) reveals no barreling within the chosen plane. Instead, interfiber sliding has taken place, producing shear offsets (Figure 11b) near the edge of the specimen. These offsets are accompanied by occasional in-plane kinks (Figure 12a), although out-of-plane kinks are more common.

Inspection of the damage region associated with the in-plane kink shows that the matrix surrounding the fibers has been essentially pulverized (Figure 12b). Fragments of fine particulate debris adhere to some of the fibers and the remaining matrix, while many of the fibers are totally devoid of any matrix constraint. Near the edge of the kink, but at the bottom of the cavity (out of range of the diamond saw), a partially

Figure 9. Out-of-plane view of out-of-plane kinks. Note specimen bulges more in this section than for in-plane section (Figure 8a). 0/90 specimen.

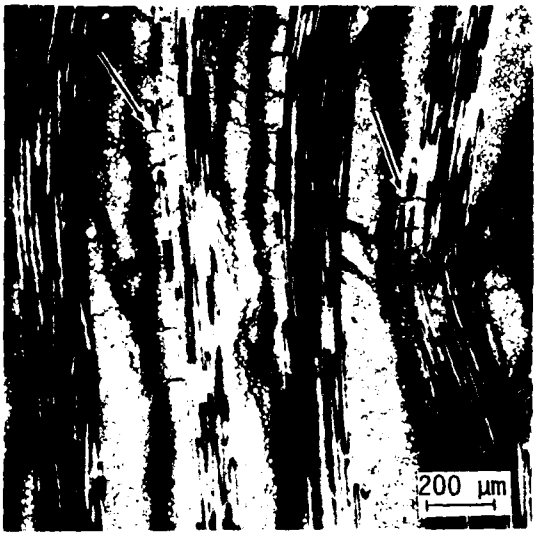

(a) Inhomogeneous kink distribution, delamination in 90° plies, and matrix microfracture (arrows) due to kinking.

(b) Broken segments of kinks, and details of 90° delamination zones.

Figure 10. Out-of-plane kink bands, 0/90 specimen.

(a) In-plane view of shear offset; *note sample displays essentially no barreling.*

(b) Close-up view of shear offset due to sliding of debonded fibers; stress axis vertical.

Figure 11. Macroscopic view of 45/45 specimen.

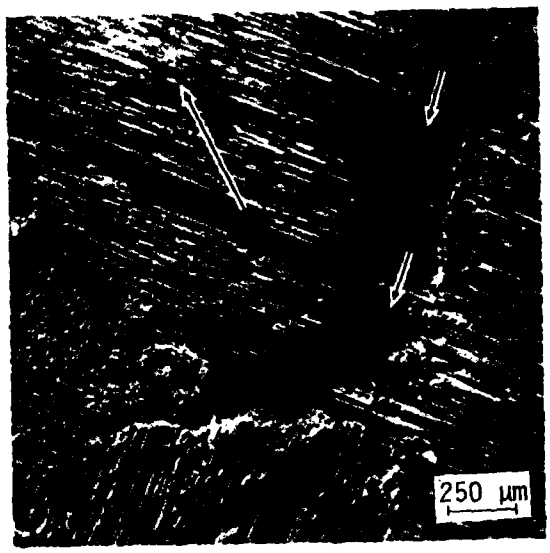

(a) Remaining kinked fibers (small arrows) indicate kink orientation.

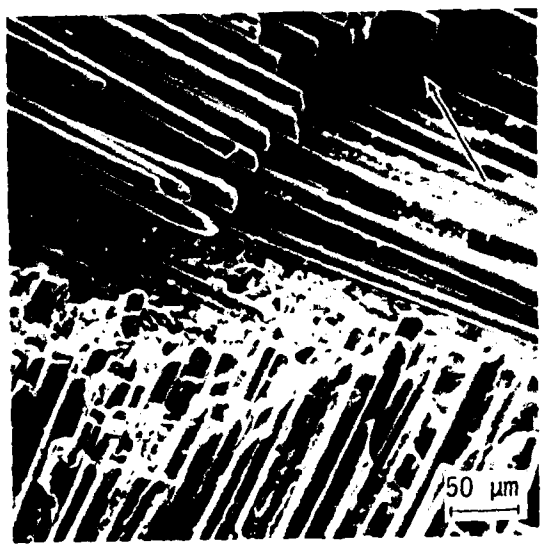

(b) Damage associated with kink; note fine particulate debris.

Figure 12. In-plane kink in 45/45 specimen (most of the kinked fibers were lost during polishing). Large arrow indicates orientation of the stress axis.

fractured fiber (arrow) can be seen (Figure 13a). This crack has the same orientation as the adjacent broken fiber directly below it. Again, the matrix material has undergone extensive microfracture during the compressive loading. Elsewhere, fiber pullout during polishing reveals (Figure 13b) compression-induced axial matrix microcracks.

In order to visualize out-of-plane kinking, it is necessary to section the specimen at 45° as shown in Figure 14a. Performing this operation (Figure 14b) does indeed show extensive out-of-plane kinking. Furthermore, the kinking is accompanied by void formation via delamination within both sets of crossplied bundles (Figure 15). This contrasts with the 0/90 situation, in which case void formation was most common within the 90° bundles.

DISCUSSION

Before considering the bases for the observed compressive strength and damage observations, it is first useful to establish the contextual significance of the parameters σ_{AE}, σ_y, and σ_c. Previous work on compressive (5) and tensile (6) failure of monolithic ceramics has shown that the present AE setup responds to two types of damage development: twinning, and microfracture. Since the present composite does not contain a twinning phase, the measured AE is considered to be caused by microfracture. Furthermore, since the fiber-matrix bond is very weak (1), it is likely that only matrix cracking or fiber fracture would provide sufficient acoustic energy to activate the transducer. Thus, σ_{AE} is explicitly assumed to denote the threshold for composite microfracture.

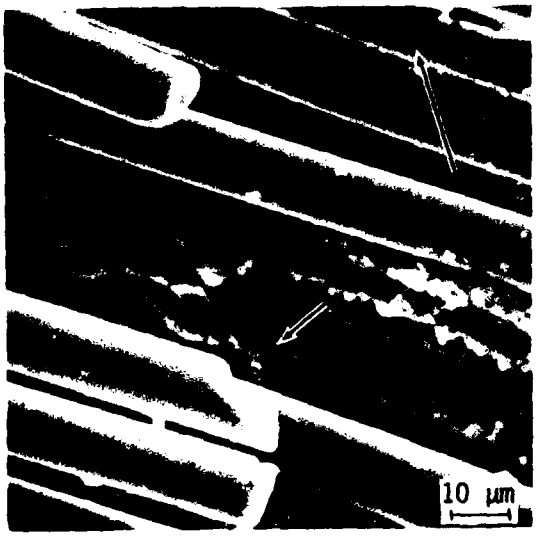

(a) Partially fractured fiber (arrow) adjacent to kink; note extensive microfracture of nearby matrix material, and presence of small particulates.

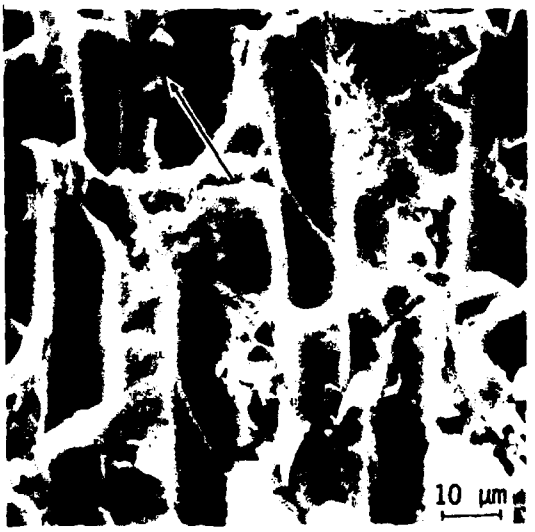

(b) Axial matrix microcracks.

Figure 13. Fiber and matrix microfracture in 45/45 specimen. Large arrow indicates orientation of stress axis.

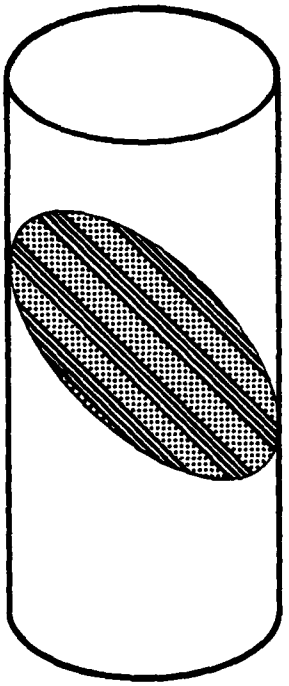

(a) Schematic

(b) 45° out-of-plane section, showing out-of-plane kinking.

Figure 14. 45°-section through 45/45 specimen.

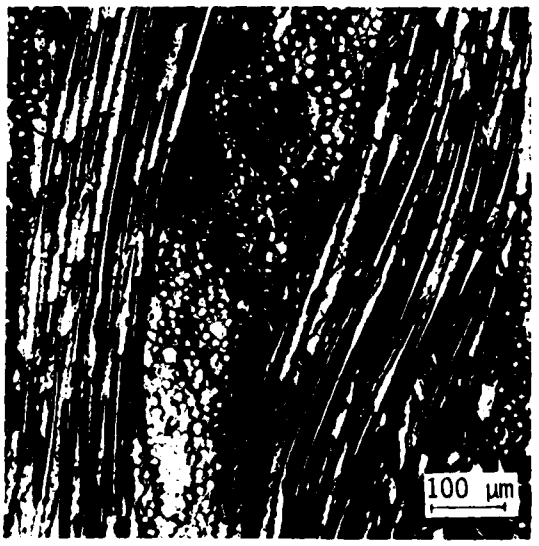

Figure 15. Out-of-plane kinking and void formation due to delamination within 0° and 90° bundles.

Earlier work has shown that such microfracture in monolithic ceramics does not produce a measurable deviation from linear stress-strain curve (5). Since the LAS matrix does not flow plastically, σ_y probably reflects a change in modulus, rather than a true "yield" point. In particular, this would occur if microcracking relaxed the matrix support of the SiC fibers to the extent that they began to flex. It is therefore postulated that fiber flexure is the basis for σ_y.

Finally, failure (σ_c) follows when instabilities set in, and the fibers begin to buckle or kink. Kinks may be either macroscopic, as for 0° orientations, or localized, as in the case of 0/90 and 45/45 tests.

Recalling Figure 3, it is clear that if these concepts are correct, then the actual details of the preceding processes must develop along somewhat different lines, in order to account for the wide discrepancies in strength for the three cases studied. Consideration of the unidirectional 0° situation, for example, suggests an initial damage state such as that sketched in Figure 16a. In this case, microfracture takes place in the LAS matrix, with cracks oriented parallel to the stress axis. Since previous work (5) has shown that such cracks in monolithic ceramics are on the order of the grain size, it is anticipated that for ceramed LAS material (2), microcracks will be only a few μm long (Preliminary study of sectioned 0° specimens which were loaded to between σ_{AE} and σ_y supports this view.). In addition, the clean fibers exposed by the compressive failure process (Figure 6b), and the fine particulate debris, on the order of a few microns in size, provide direct evidence for fine-scale matrix microfracture. It should be noted that under compression, clean fibers cannot result from pullout, as for tension.

For 0/90 material, a totally different scenario develops, which is basically documented in Figure 10. In this case, microfracture will not develop in the 0° bundles, since the unidirectional 0° experiments show that such bundles should not microfracture below a stress of ∿600 MPa. Therefore, the lower failure strength for 0/90 specimens must relate to a low microfracture threshold for 90° bundles.

It is proposed that such fracture occurs as indicated in Figure 16b. The SiC fibers are much harder than the LAS matrix, so that the latter is essentially compressed between the fibers in what might be considered a combined microcompression/microhardness test. Matrix cracks form in the indentation fields beneath the SiC "indenters", and then join to connect the fibers. Since the matrix-fiber interfacial strength is very low (1), it is easy for the fibers to debond, which creates the large void-like cracks shown in Figure 10. As this process proceeds, the 0° fibers lose their support, flex (σ_y), and finally begin to kink and buckle.

The situation is very similar for the 45/45 composites as well; cracks form the same way, but here, <u>both</u> sets of plies crack as shown in Figure 16b. Furthermore, there are no 0° fibers to provide partial support, and the composite fails at a predictably low stress level.

Since none of these failure processes are strongly dependent upon fiber-matrix interface properties, and since this is the only significant difference between LAS-I and LAS-II, it is not surprising that compressive strengths for 0/90 and 45/45 orientations (Figure 4) are basically independent of matrix chemistry. In essence, the same failure processes operate in each material at about the same stress levels. What does seem

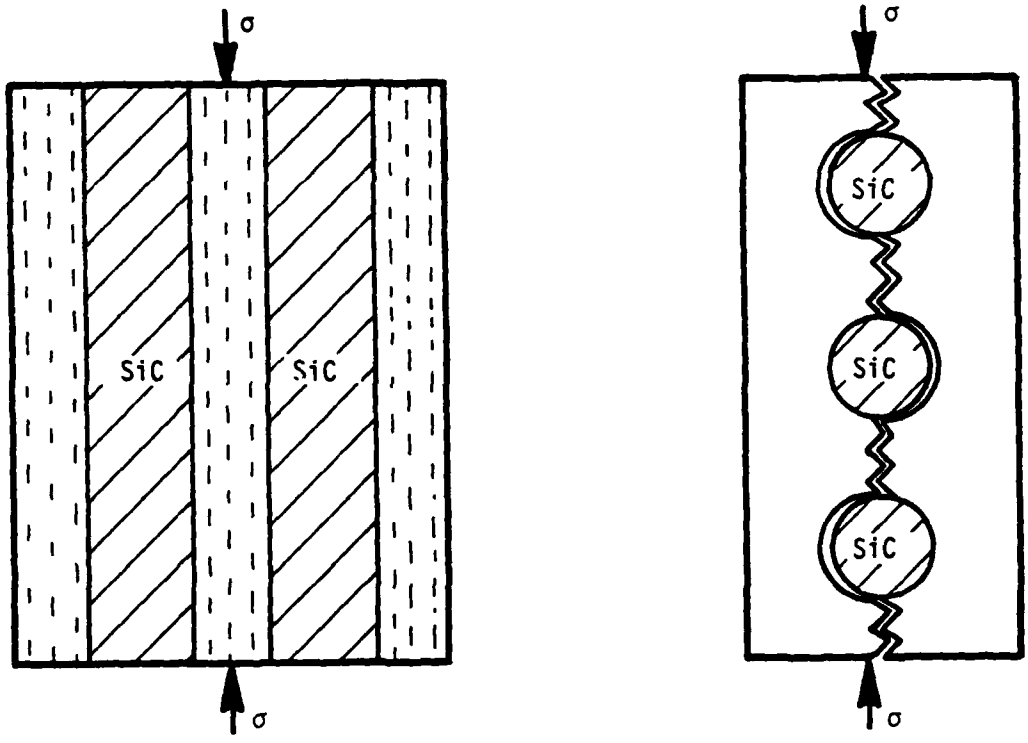

(a) 0° plies; grain-size microcracking within LAS matrix.

(b) 90° and 45° plies; fiber debonding and LAS microfracture on scale of fiber spacing.

Figure 16. Schematic of postulated microfracture in various layup configurations relative to compressive stress axis.

surprising is that compressive strengths for the two matrix variants differ for unidirectional 0° tests.

However, it should be borne in mind that the specimen configurations were quite different. In particular, the larger dogbone specimens used in the LAS-I experiments (1) probably had a greater tendency to buckle than the smaller, stubbier cylindrical specimens used in testing the LAS-II material. The higher the stress level attained, the greater would be the tendency for the more unstable specimen to buckle. Since the 0° configuration afforded to greatest intrinsic strength, it is reasonable that this situation would be most susceptible to specimen instability. It is interesting in this regard that the LAS-I 0° specimen exhibited a tendency to fail in shear (1), while the LAS-II (cylindrical) specimens barreled isotropically, and failed by macroscopic kinking. At lower stresses, the dogbone configuration would have been stable, hence the agreement between the 0/90 and 45/45 results for LAS-I and LAS-II.

As indicated in Figure 5, the compressive strength for LAS-II was roughly equivalent to that obtained for four-point bend tests in Ar at all temperatures, and equivalent to four-point flexure data in air for temperatures less than ∿600C (1). It was noted by Prewo (1) that in air at 23C, failure of the bend specimens initiated on the compressive sides (one assumes the same would hold for Ar as well). Thus, the present results are in excellent agreement with that observation. Although undocumented, it seems likely that the flexural specimens continue to fail in this fashion at elevated temperature as long as the environment is relatively inert, while compressive failure is normally environment insensitive.

However, air at elevated temperatures causes preferential embrittlement of tensile-loaded LAS matrix material (1). This embrittlement explains the rapid dropoff in four-point flexural strength in air at 900-1000C, which probably shifts the failure mode from compressive to tensile as the tensile damage threshold is lowered.

Temperature does not have a strong influence upon compressive strength of LAS-I or LAS-II. However, this is reasonable, in view of the apparent predominant role of matrix microfracture in the failure process. Since matrix softening does not occur until temperatures on the order of 1000C are attained, the basic microfracture-controlled failure processes should be relatively unaffected over the temperature range considered.

This work clearly implicates the properties of the matrix as the central factor in compressive failure, which ultimately takes place by means of macro- or micro-kinking. Evans and Adler (4) analyzed compressive kinking theoretically, and showed conclusively the central role of matrix yield strength on kink suppression. In the present context, matrix microfracture would substitute for matrix yielding. The analysis (4) also showed that matrix voids, such as those due to delamination in 90° bundles for 0/90 tests, lead to the premature buckling and kinking of 0° fibers aligned with the stress axis.

CONCLUSIONS

1. The critical event which controls compressive failure is matrix microfracture.

2. The compressive stress level for matrix microfracture is controlled by composite macrostructure and microstructure.
3. Kinking is a result of, and accommodated by, matrix microfracture.
4. Fiber-matrix interface strength is not a critical factor in compressive microfracture and associated void development, unless it could be made much higher than that for the current LAS formulations.

REFERENCES

1. K. M. Prewo, "Advanced Characterization of SiC Fiber Reinforced Glass-Ceramic Matrix Composites", ONR Technical Report, Contract No. N00014-81-C-0571 (June 1983).
2. J. J. Brennan, "Additional Studies of SiC Fiber Reinforced Glass-Ceramic Matrix Composites", ONR Technical Report, Contract No. N00014-82-C-0096 (February 1983).
3. M. R. Piggott, "A Theoretical Framework for the Compressive Properties of Aligned Fibre Composites", J. Mat. Sci., 16 (1981) p. 2837-2845.
4. A. G. Evans and W. F. Adler, "Kinking as a Mode of Structural Degradation in Carbon Fiber Composites", Acta Met., 26 (1978) p. 725-738.
5. J. Lankford, "Compressive Strength and Microplasticity in Polycrystalline Alumina", J. Mat. Sci., 12 (1977) p. 791-796.
6. J. Lankford, "Tensile Failure of Unflawed Polycrystalline Alumina", J. Mat. Sci., 13 (1978) p. 351-357.

Journal of Materials Science (submitted)

II.
DEFORMATION AND FRACTURE OF YTTRIA-STABILIZED ZIRCONIA SINGLE CRYSTALS

James Lankford
Southwest Research Institute
San Antonio, TX 78284

ABSTRACT

Deformation and failure mechanisms are characterized for fully and partially yttria-stabilized single crystals tested in compression from 23C to 1150C. It is found that both types of material exhibit extensive plastic flow over most of this temperature range, producing rapid decreases in strength with increasing temperature. Tetragonal to monoclinic transformation-induced plasticity is not observed; rather, plastic flow is related solely to dislocation activity. Evidence is found for apparent cubic to rhombohedral transformation during polishing, and reverse rhombohedral to cubic transformation during imposed compressive stress.

INTRODUCTION

Considerable interest has focussed upon partially stabilized zirconia single crystals (1-3), which appear to possess a number of desirable technological properties. For example, these materials maintain their flexural strength to temperatures as high as 1500C, their fracture toughness at elevated temperature increases with temperature, and they lack grain boundaries and grain boundary phases which tend to promote intergranular failure at elevated temperature. Questions persist, however, regarding the role of stress-induced transformations in the strengthening and toughening of these ceramics, as opposed to polycrystalline MgO- and CaO-partially stabilized zirconias, in which transformation-induced plasticity clearly is very important. Similarly, the relevant deformation and damage processes are not well understood. Finally, most of the work to date has involved a nominally tensile stress state, while certain technological applications, such as high temperature bearings, will involve compressive or multiaxial loading. The present study seeks to address some of these issues.

Certain experimental results by other researchers provide an important background in this regard, particularly the papers by Ingel, et al (1,2), based on the dissertation by Ingel (4), dealing with the mechanical properties of zirconia crystals stabilized with from 3 to 20 wt.% Y_2O_3. Over most of the temperature range 23C to 1500C, the strengths and fracture toughnesses of partially stabilized variants, i.e., ones with significant amounts of tetragonal phase ($<$ 20 wt.% Y_2O_3), considerably exceeded those for fully stabilized (cubic, $\gtrsim$ 20 wt.% Y_2O_3) crystals. It was found further (2,4) that partially-stabilized (6 wt.% Y) bend specimens evidenced very little plasticity, even for temperatures as high as 1500C.

Cubic crystals, on the other hand, underwent a brittle ductile transition at around 1000C to 1200C; at 1500C, fracture could be either brittle or ductile, with from zero to 7.8% permanent strain, depending upon crystallographic orientation.

The fracture toughness of both partially and fully stabilized crystals decreased with increasing temperature up to ~1000C, above which (roughly the maximum temperature for the tetragonal-to-monoclinic transformation) K_{IC} was found to increase with temperature. The former effect was ascribed to reduction in toughening contributed by the tetragonal-to-monoclinic phase transformation, which was assumed to be operating. The high temperature toughening was considered to be caused by crack-precipitate interactions, as reflected in the rough fracture surfaces of the PSZ specimens, and the smooth fractography of the fully stabilized ones. Michel, et al (3), likewise found predominantly tetragonal 5.4 wt.% Y-ZrO_2 crystals tested at 23C to be ~3 times tougher than the cubic phase (16.2 Y) material; however, Raman spectroscopy showed conclusively that the fracture surfaces of the specimens contained no monoclinic phase. Thus, the tetragonal-to-monoclinic transformation could not be responsible for the PSZ toughness. Instead, the greater toughness of the tetragonal phase crystals was attributed to a rough fracture mode (faceted on {001}), versus smooth cleavage on {111} for the cubic phase.

Interesting work related to these experiments was performed by Coyle, and described in his recent dissertation (5). By also utilizing Raman spectroscopy, Coyle determined that the fracture surfaces of 6 wt.% Y-PSZ specimens failed in compression and in bending evidenced monoclinic transformed layers 50 μm and 15 μm thick, respectively. On the other hand, 5 wt.% Y-PSZ failed in bending had no monoclinic material on its fracture

surface. These experiments demonstrate the sensitivity of the transformation process to stabilizer chemistry and precipitate microstructure.

Slip systems in yttria cubic stabilized zirconia (Y-CSZ) and MgO stabilized PSZ (Mg-PSZ) were studied by Hannink and Swain (6). From hardness anisotropy, it was inferred that for both Y-CSZ and Mg-PSZ crystals, the active slip system over 23-600C is either {001}<011> or {111}<110>. Based on an earlier study of CaF_2 (7), and a TEM study (8) of Ca-CSZ crystals deformed at 1350C, it was assumed that the current system was {001}<011>. However, it was observed that Arrhenius plots of hardness versus reciprocal temperature showed a distinct break at around 400C, which normally indicates a change in thermally activated mechanism. As noted by the authors (6), this might be taken to suggest activity on another slip system.

Recent work by two independent groups in Japan has revealed (9,10) a possible additional, complicating factor. Based on X-ray diffraction, it was determined that the cubic phase, for both Y-PSZ and, to a lesser extent, Y-CSZ, apparently can transform to a rhombohedral structure. This transformation occurs both by grinding/polishing (9), i.e., in thin surface layers, and also in the bulk (10), for certain compositions and, probably, certain heat treatments. It appears that the rhombohedral phase is quite unstable, and that the cubic → rhombohedral transformation is stress-assisted and reversible (10).

In order to explore the interrelationships between these factors, an experimental program was performed involving compressive deformation of both fully and partially stabilized Y-ZrO_2 crystals. Since compressive microfracture is a relatively stable process, it is possible to generate

damage under high stresses within the bulk of a specimen without failing it. This facilitates subsequent damage characterization, which is otherwise quite difficult to accomplish for the extremely localized high stress regions attending crack tips, or their flanks, in tensile specimens.

EXPERIMENTAL PROCEDURE

Materials for specimens were provided by R. W. Rice of NRL, the crystals deriving from the same as-received batches* used in the work of Ingel (4). Two compositions were studied, namely, 20 wt.% Y_2O_3-ZrO_2, and 5 wt.% Y_2O_3-ZrO_2; both are fully characterized by Ingel (4). Briefly, however, the former were fully stabilized, and therefore had a cubic microstructure, while the latter consisted of a "tweed" microstructure, composed of ~50 volume fraction of tetragonal precipitates within a cubic matrix. The precipitates are coherent or semicoherent with the cubic matrix, and form distorted ellipsoids ranging in length from ~400 nm to ~1400 nm, and in width from ~80 nm to ~280 nm (4). Ambient material condition properties of both compositions are given in Table I, together, for comparison, with corresponding properties for polycrystalline Mg-PSZ** tested earlier in compression (11).

Compression specimens in the form of right circular cylinders, ~9 mm long x 4.5 mm diameter, were machined from the crystals. The axis of each specimen was oriented near the center of the standard cubic stereographic

---

*CERES Corporation, Waltham, MA.

**Nilsen TS-Grade PSZ; Nilsen Sintered Products, Ltd, Northcote, Victoria, Australia.

TABLE I

MATERIAL PROPERTIES

Material	Flexural Strength (MPa)	Hardness (GPa)	Fracture Toughness (MPa$\sqrt{m}$)
20Y-CSZ Single Crystal	196	15.3	1.9
5Y-PSZ Single Crystal	1384	13.6	6.9
Mg-PSZ Polycrystal	600	10.2	8-15

triangle, and provided approximately equal Schmid factors of approximately 0.45 for {001}<011> and {111}<110> slip. The ends of both the specimens and their alumina loading platens were precision ground and lapped parallel to within 2 μm.

Compression tests were performed in air at a strain rate of $7x10^{-5}sec^{-1}$, over a temperature range of 23C to 1150C. In order to establish the threshold stress level for microfracture, an acoustic emission system was employed, as described in conjunction with a recent study of polycrystalline Mg-PSZ (11).

To facilitate damage characterization, extremely smooth (0.05 μm diamond) flats were polished onto certain specimens, which were subsequently loaded past yield, and then unloaded. The flats were then examined using Nomarski microscopy and scanning electron microscopy (SEM) of palladium-coated flats, and transmission electron microscopy (TEM) of two-stage carbon surface replicas. Finally, some of these specimens were sectioned normal to their axes into thin wafers, which were ion-milled and examined as thin foils in the TEM.

RESULTS

In the following section, the deformation and fracture of single crystal 20Y-CSZ and 5Y-PSZ are compared with one another, and with polycrystal Mg-PSZ (11). Relevant damage mechanisms are then presented.

Deformation and Failure Behavior

For 20Y-CSZ, fracture is brittle at 23C (Figure 1); crystal orientation is indicated by the stereographic triangle. However, as the test temperature rises, the material yields and flows, with the plastic strain

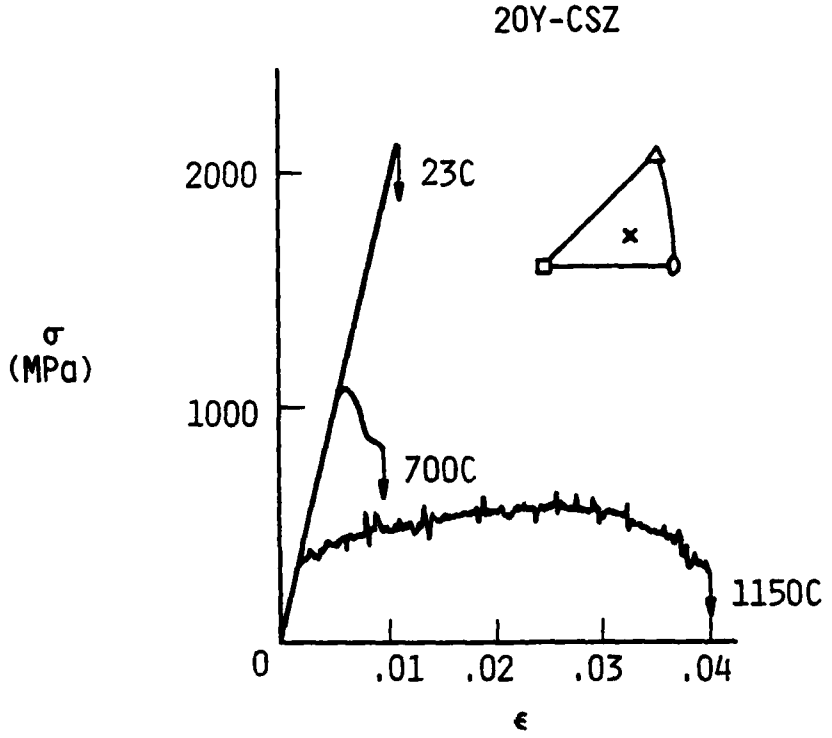

Figure 1. Compressive stress versus strain for 20Y-CSZ single crystal.

at failure approaching 4% at 1150C. At the latter temperature, the crystal hardens very little, and plastic flow is "jerky".

On the other hand, 5Y-PSZ (Figure 2) fails following plastic flow at 23C, and at this temperature is considerably stronger than cubic material under equivalent conditions. The strength of the partially stabilized ceramic decreases quite rapidly with increasing temperature, while the extent of plastic flow concurrently increases, reaching nearly 7% at 1150C. For temperatures $\gtrsim$ 250C, flow is again rather jerky.

By way of comparison, the strength of polycrystalline Mg-PSZ (Figure 3) is essentially independent of temperature to 1000C (11). Like the single crystals, however, this material also exhibits plastic behavior; this flow is serrated, the amplitude of the local load drops increasing with temperature.

It is interesting that the single crystals emit no acoustic emission (AE) prior to yielding. In a few cases, AE was detected after several percent plastic strain, although the most common observation was little or no AE until failure. Similarly, the polycrystalline material exhibited AE for stresses above yielding, but below ultimate, only for temperatures $<$ 500C, above which only the failure event itself yielded detectable stress waves (11). These results suggest that significant flow takes place prior to the nucleation of microcracks; subsequent microscopy will show that this is indeed the case.

The temperature dependence of yield strength (σ_y) is summarized for all three materials in Figure 4. Here the continuously decreasing plastic flow resistance of both fully and partially stabilized zirconia contrasts with the essentially constant strength polycrystalline material. Ultimate compressive (σ_c) strengths follow the same qualitative trends (Figure 5),

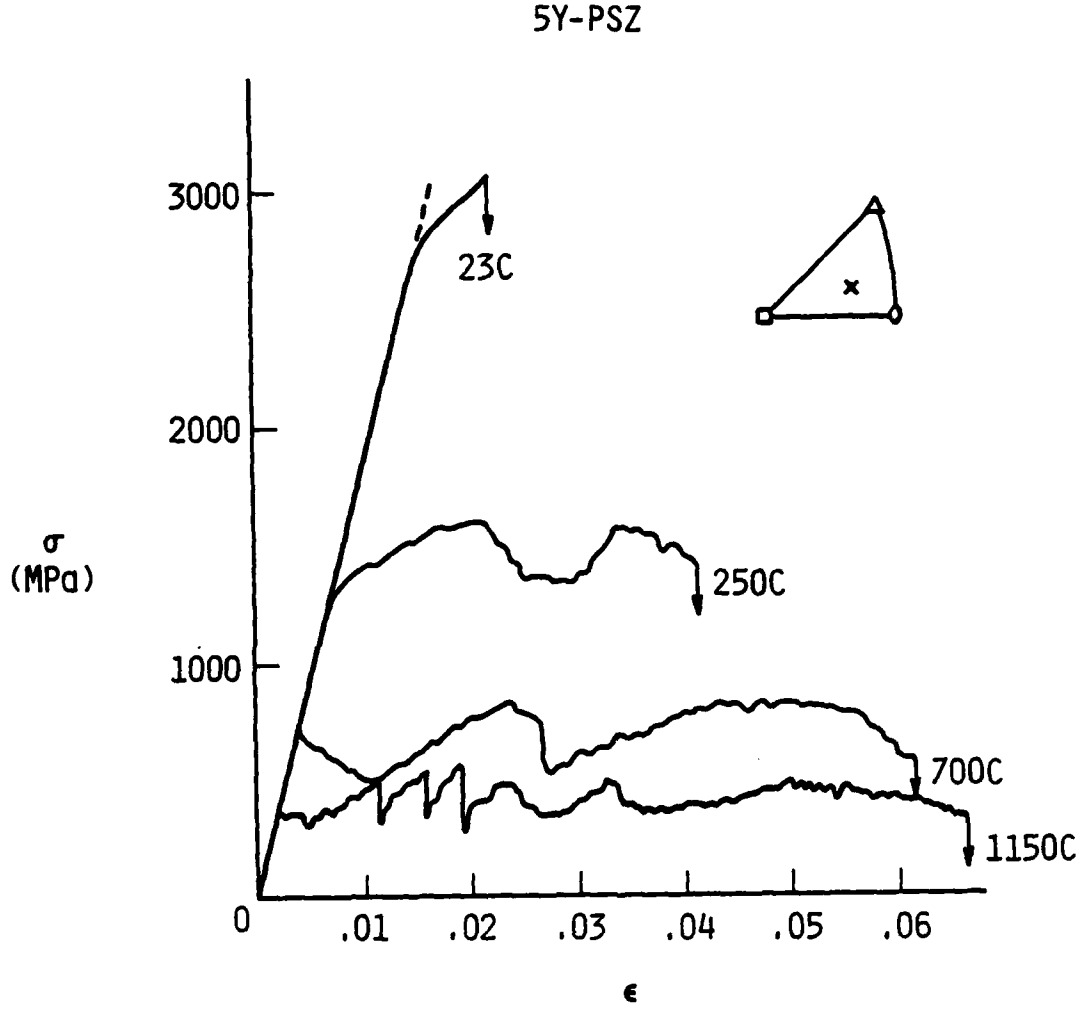

Figure 2. Compressive stress versus strain for 5Y-PSZ single crystal.

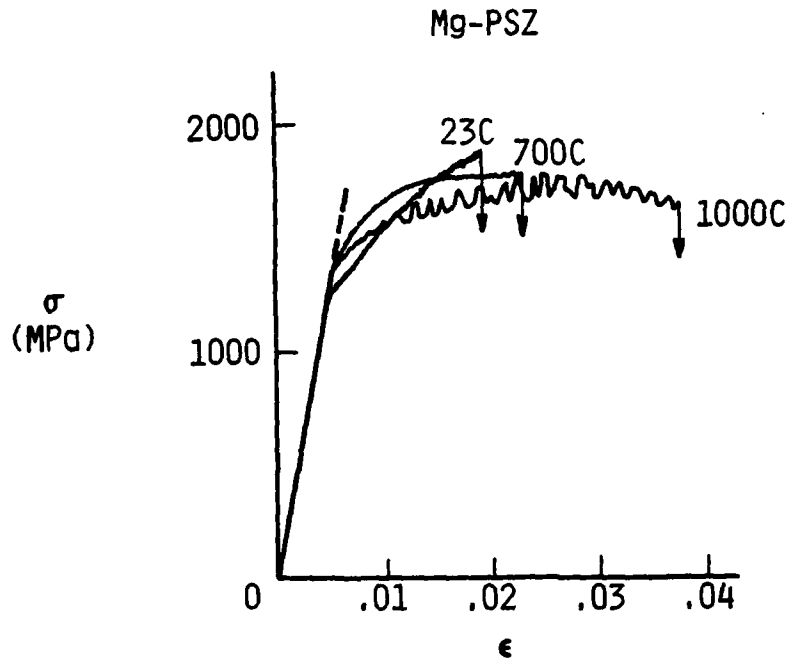

Figure 3. Compressive stress versus strain for polycrystalline Mg-PSZ.

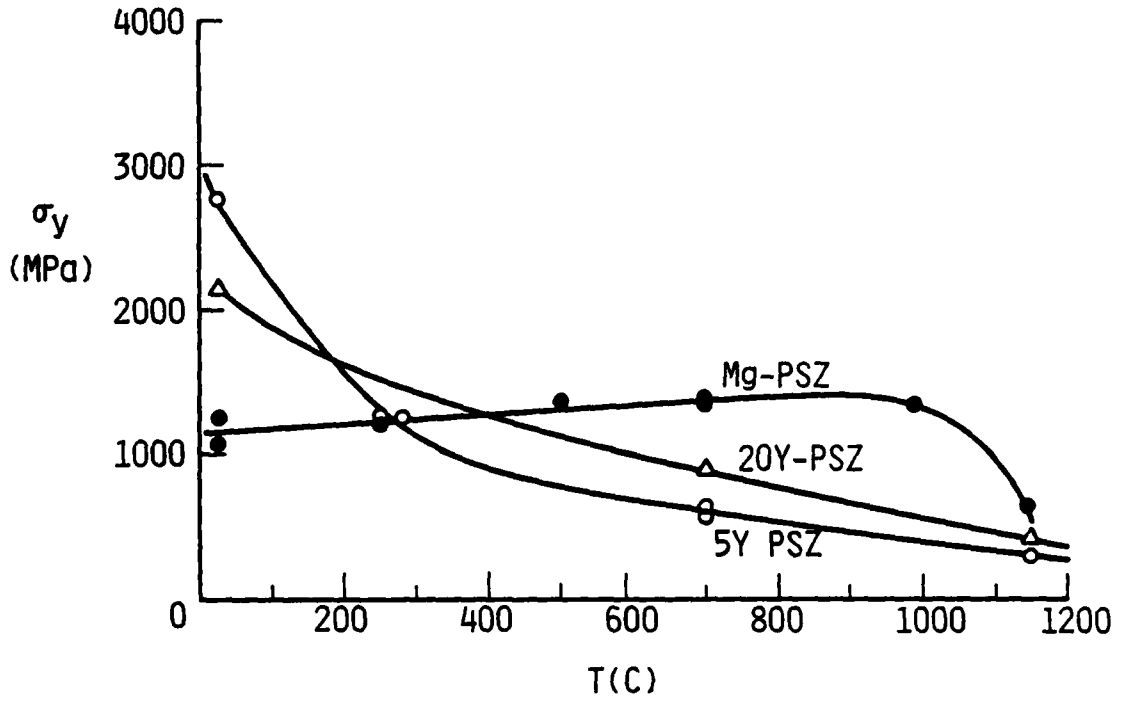

Figure 4. Yield strength versus temperature for all three ceramics.

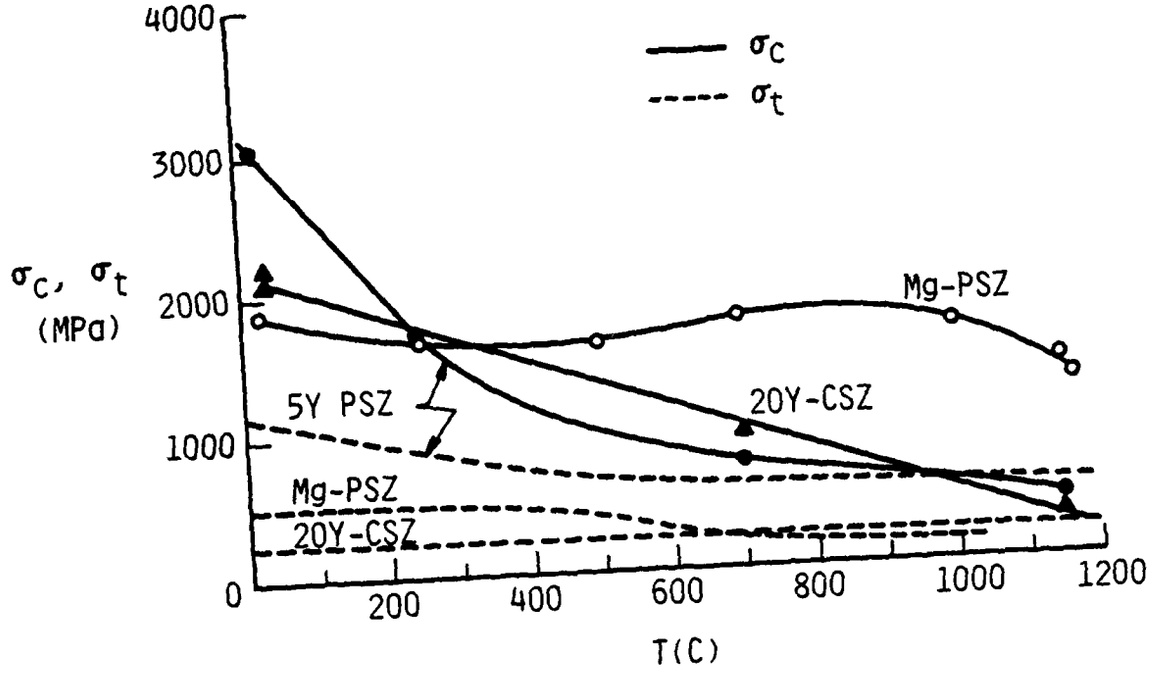

Figure 5. Compressive and flexural strength versus temperature for all three ceramics.

while flexural strengths (σ_t) decrease only slightly with increasing temperature. Particularly noteworthy is the fact that while $^{\sigma}c/\sigma_t \simeq 4$ for polycrystalline Mg-PSZ from 23C to 1200C, the same ratio for 20Y-CSZ and 5Y-PSZ drops from ~8 and ~3, respectively, at 23C, to ~1 at T ≈ 1000C. The value of $^{\sigma}c/\sigma_t$ for brittle materials is usually about 8; it will be recalled that within the present series of tests, only 20Y-CSZ at 23C exhibited brittle failure.

Figure 6 shows strain to failure for all three materials over the temperature range 23C to 1200C. It is clear that despite similarities in $\sigma_y(T)$ and $\sigma_c(T)$, plastic deformation in 5Y-PSZ differs both in its extent and, possibly, its mechanism, from that of 20Y-CSZ. As discussed in the next section, the latter seems to be true.

Deformation and Fracture Mechanisms

It was shown elsewhere (11) that polycrystalline Mg-PSZ fails by the nucleation, during plastic flow, of a myriad of tiny, grain-sized, axial microcracks, which eventually combine to cause failure. Their sudden coalescence usually causes the specimen to essentially explode. The single crystals studied here behaved in a decidedly different fashion; for purposes of example, photomicrographs of specimens tested at 700C are used, results at other temperatures differing chiefly in degree.

Specimens compressed to failure, i.e., a state of negligible load-bearing capacity, are shown in Fig. 7(a) and 7(b). The 5Y-PSZ crystal fails by sliding on several distinct, macroscopic shear planes, while the 20Y-CSZ specimen has failed due to the coalescence of multiple shear microcracks, following extensive plastic flow within the shear bands. It should be noted that the latter specimen is still intact. Part of the path each

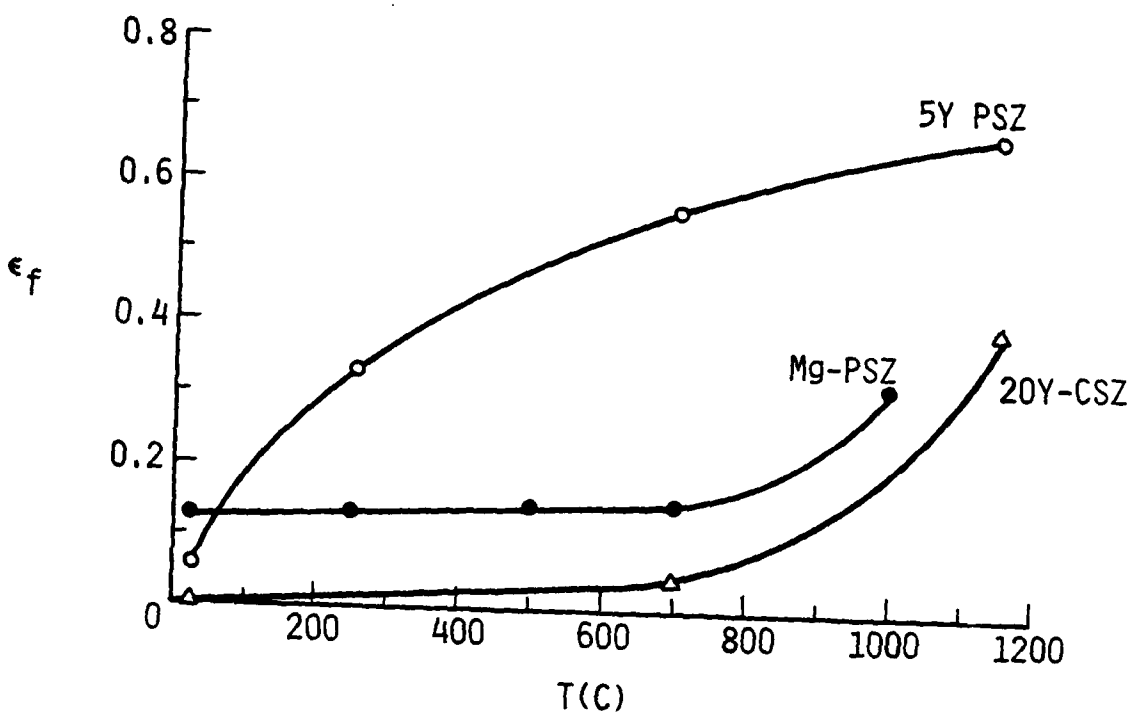

Figure 6. Strain at failure versus temperature for all three ceramics.

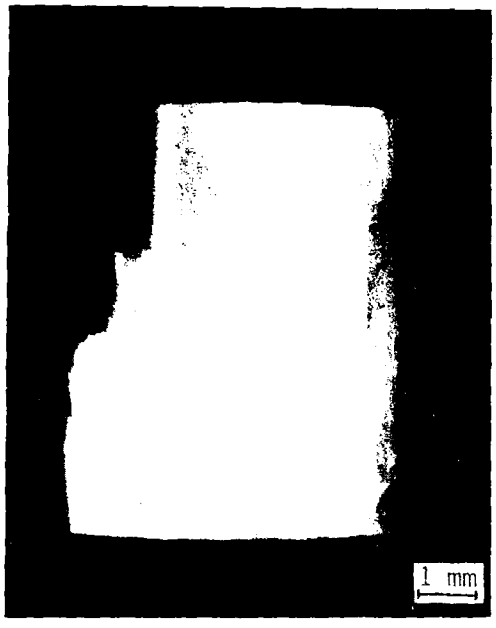

(a) Shear fracture, 5Y-PSZ, 700C.

(b) Fracture by coalescence of multiple shear microcracks, 20Y-PSZ, 700C.

(c) Planar slip bands, 5Y-PSZ, 700C, ε_p = 1.5%.

(d) Apparent wavy slip bands (arrow), 20Y-CSZ, 700C, ε_p = 1.5%.

Figure 7. Macroscopic views of fracture and deformation in 5Y-PSZ and 20Y-PSZ.

of these specimens followed to failure is shown in Fig. 7(c) and 7(d), which represent specimens compressed to 1.5% plastic strain (ε_p).

At this juncture the 5Y-PSZ crystal has slipped on planar slip bands over some three-quarters of its length, with the bands having progressed from the lower end of the specimen. Not readily visible in the photo are macroscopic twins near the upper end, which share the same crystallographic trace as the slip bands. The 20Y-CSZ specimen, on the other hand, has developed what might best be described as wavy deformation bands (arrow), and no twins. Also visible in the Nomarski illumination are what appear to be an array of surface dimples. Axial microcracks are not present on either specimen.

Higher magnification views of these specimens reveal interesting details. For example, the twins in the upper portion of Fig. 7(c), shown in Fig. 8(a), apparently extend almost all the way across the specimen. Furthermore, they are superimposed upon what appear to be rather coarse polishing marks -- scratches which appear far too coarse to correspond to a 0.05 μm finish. The planar slip bands shown in Fig. 8(b) lie in an identical field of scratches. Since the polishing marks outside of the slip band field are sharper than those within it, it would appear that the formation of the scratches preceded the slip bands.

This is not as trivial a statement as it might seem, because the "polishing marks" were invisible prior to the test. Figure 9 shows a Nomarski view of a polished flat on an untested 5Y-PSZ specimen. Evidently, compressive stress caused the polishing marks to become visible, and apparently prior to extensive plastic deformation.

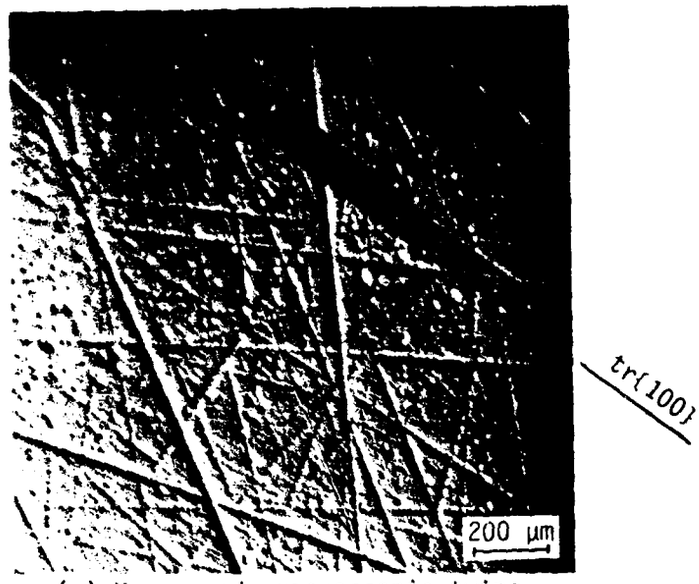

(a) Upper end, macroscopic twins.

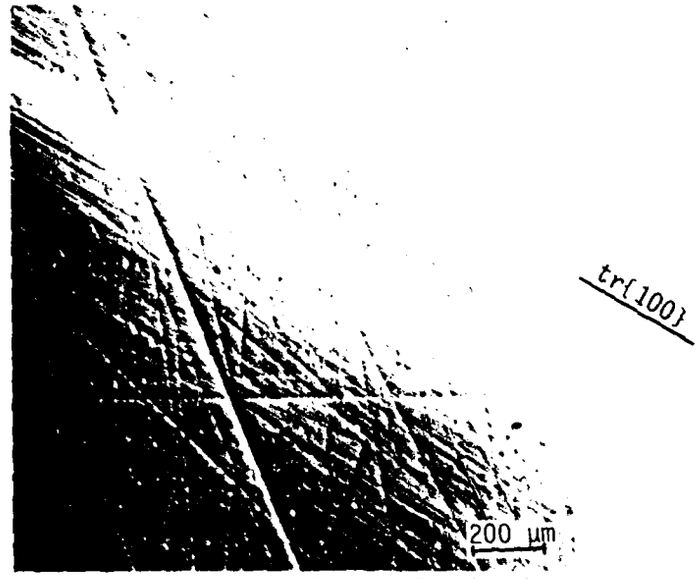

(b) Upper edge of planar slip bands.

Figure 8. High magnification Nomarski photos of 5Y-PSZ specimen shown in Fig. 7(c), T = 700C, ϵ_p = 1.5%. Slip bands and twins superimposed on polishing marks.

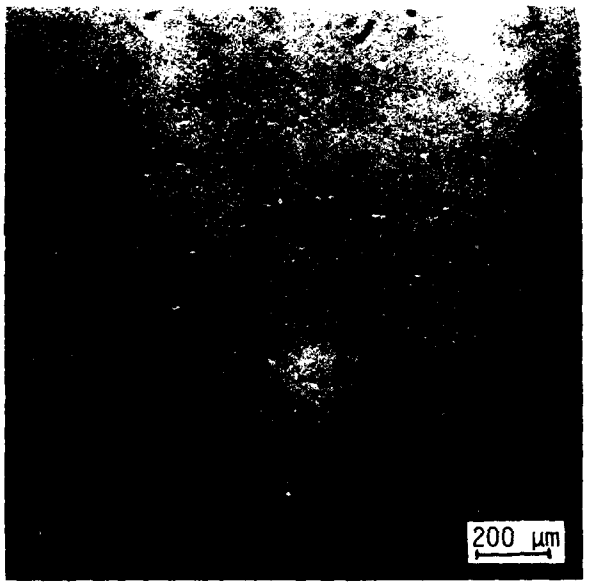

Figure 9. Polished flat, Nomarski illumination, 5Y-PSZ, prior to test (no deformation).

Laue X-ray diffraction was used to establish the crystallography of the twins and the slip bands. It was determined thereby that the planar slip system was {001}<011>, and that the trace of the twin planes was {001}.

Deformation details of the cubic zirconia were strikingly different. As shown in Figure 10, intense wavy slip bands seemed to lie predominantly along {111}; however, these were connected by diffuse secondary slip bands with an unusual "feathery" appearance, as shown in Fig. 10(b). Polishing scratches again are visible, but only major ones, and these seem to be made up of rows of dimples. Looking again at Fig. 8, it can be seen that these polishing marks are likewise formed of dots, but they are much smaller and closer together than for the cubic material.

The preceding observations suggest that some sort of transformation must occur within both CSZ and PSZ due to the imposition of compressive stresses. Transmission electron microscopy of 5Y-PSZ surface replicas shadowed at very low angles indicates that transformations also occur during polishing as well (Figure 11). Here the optically smooth surface can be seen to be covered, over about 50% of its area, with small, rumpled, apparently transformed domains. Close inspection indicates that some of these may be internally twinned.

Compressive deformation causes further transformation, as shown in Figure 12(a). In this case, it appears that the transformed particle density is not as great as in Figure 11, suggesting that the polishing-induced transformation may revert under the action of compressive stress. Close observation of polishing marks shows that they are actually composed of clusters of transformed microdomains — the "dots" seen in Figs. 8 and

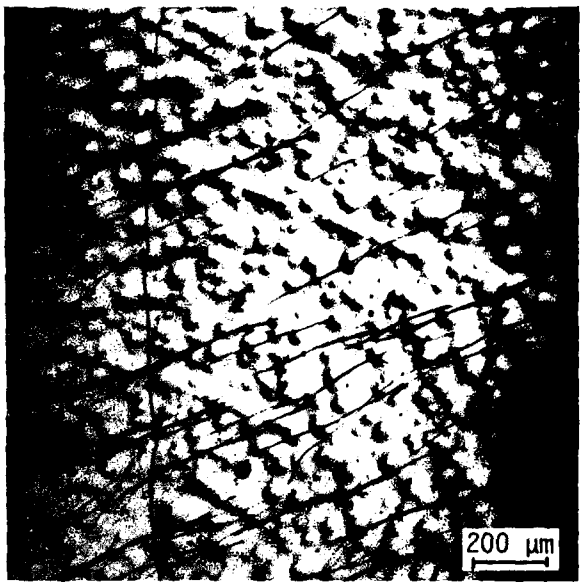

tr{111}

Figure 10. High magnification Nomarski photos of 20Y-CSZ specimen shown in Fig. 7(d), T = 700C, ε_p = 1.5%. Slip bands superimposed on polishing marks and dimples.

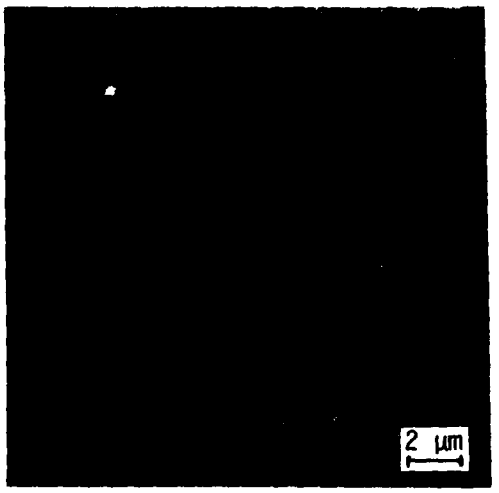

Figure 11. TEM replica, 5Y-PSZ, undeformed; surface rumpling due to transformations induced by polishing (same surface as that in Figure 9).

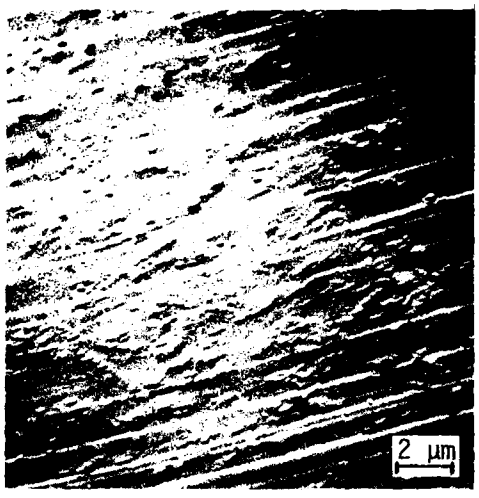

(a) Overall view, slip bands and surface rumpling caused by transformations.

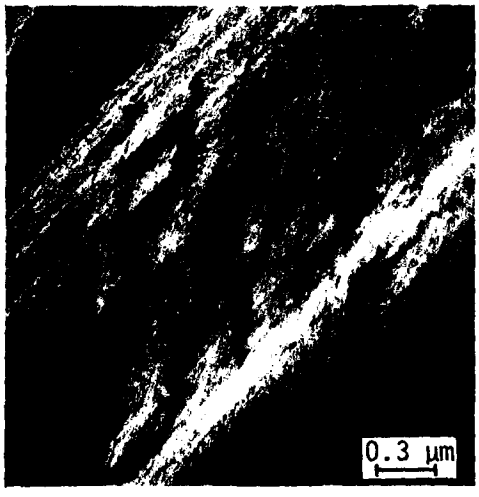

(b) Slip band microstructure, shape and internal structure of transformed microdomains.

Figure 12. TEM replica, 5Y-PSZ, 700C, ϵ_p = 1.5%.

10. Study at high magnification (Fig. 12(b)) shows that the slip bands are composed of numerous close-spaced slip lines, and that the transformed particles have a distinct internal structure.

Raman spectroscopy was used to evaluate the phases present on the 5Y-PSZ flat shown in Fig. 8. Careful study showed absolutely no monoclinic phase, indicating that the transformations which reveal the scratches are not of the type tetragonal → monoclinic.

Transmission electron microscopy of both undeformed (4) 5Y-PSZ specimens and ones deformed in compression at 283C (Fig. 13(a)), shows a "tweed" structure composed of cubic and tetragonal domains. Dislocations (arrows) are visible in the deformed structure; further TEM work is in progress to establish whether they lie within the active {100}<110> slip system.

At 700C, and a plastic strain of ~1.5% (versus the preceding ~0.5%), the microstructure is highly distorted, as shown in Fig. 13(b) and (c). The original "tweed" structure is very difficult to recognize, and domains appear faulted; by changing the diffraction conditions, what appear to be extended partial dislocations (arrows, Fig. 13(c)) can be discerned lying on certain faults.

Interestingly, preliminary TEM study of polycrystalline Mg-PSZ compressed to a strain of ~0.5% at 23C shows no evidence of dislocation activity. However, the lattice is highly strained by tetragonal to monoclinic transformations, so that any dislocations would be very difficult to distinguish.

(a) T = 283C, ε_p ≈ 0.5%; tweed microstructure, arrows indicate dislocations.

(b) T = 700C, ε_p ≈ 1.5%; distorted and faulted microstructure.

(c) Altered contrast, same region as in (b), showing possible extended dislocations (arrows) in fault.

Figure 13. Transmission electron microscopy of deformed 5Y-PSZ. Foils are normal to stress axis.

DISCUSSION

The preceding results are surprising and interesting in a number of ways, with regard to both mechanical behavior and microstructural development. Furthermore, they may have implications with regard to other factors such as fracture toughness.

The extreme temperature sensitivity of σ_y and σ_c for both 5Y-PSZ and 20Y-CSZ is at variance with the equivalent tensile strengths. This is probably due to the fundamentally different processes involved in tensile and compressive failure. During a tensile test, the stress field may cause very limited plastic flow, as observed by Ingel, et al (1,2), but before this becomes a factor, i.e., before plastic instability can set in, the specimen inevitably fails by nucleating a single fatal crack at some intrinsic flaw. Since the latter process is not affected by a slight amount of general plastic flow, σ_T is relatively independent of temperature.

During compression, however, microcracks do not form until considerable plastic strain has accumulated. Since no grain boundaries are available to block slip lines, flow takes place in continuous bands across the specimen; shear cracks eventually form within the slip bands, and the specimens lose their load bearing capacity (fail). This process is facilitated in 5Y-PSZ by the semicoherent nature of the tetragonal precipitates and their cubic parent phase. As the tetragonal $^c/_a$ ratio is nearly unity, the slip process is basically occurring in a cubic system, which permits planar slip. As the temperature rises, slip becomes easier, and plastic instability (Figure 7(a) and (b)) sets in at progressively lower stress.

The fact that $\sigma_C \simeq \sigma_T$ for $T \gtrsim 900C$ is probably coincidental, since failure is achieved by entirely different mechanisms. This contrasts with the case for polycrystalline ceramics (11-13), in which failure in both tension and compression involves subcritical tensile microcracks. The latter are simply harder to nucleate and propagate in compression, so that σ_C/σ_T is consistently $\gtrsim 4$ for such materials.

In an earlier paper (14), it was concluded that the serrated "flow" of polycrystalline Mg-PSZ was caused by cooperative shear of tetragonal particles producing bands of transformed monoclinic material. Since this process is not very sensitive to temperature, and since failure occurs by the usual mechanism of nucleation and coalescence of axial microcracks, $\sigma_C/\sigma_T >> 1$ over a wide range in temperature. However, for the single crystal materials, the flow stress load drops probably have a different origin, namely, the sequential activation of individual planar (5Y-PSZ) and wavy (20Y-CSZ) slip bands. In this case the serrations are extremely relevant, as they represent events which are directly responsible for the development of the plastic instability which leads to failure.

With this point in mind, it is obvious that crystallographic orientation probably was important in the failure of the single crystals. The chosen orientation amounted to provision of the possibility of easy glide on essentially any low-index slip system. For the 5Y-PSZ material, it would be interesting to explore the effect of testing crystals in orientations for which {001}<011> is hard to operate, the hardest being {001} aligned with the compression axis. If the activation of a secondary system such as {111}<110> were sufficiently difficult, the crystals would be forced to fail in a brittle fashion, i.e., by nucleating axial microcracks.

The compressive strength would then be much less sensitive to temperature, and should more-or-less maintain its ambient strength as the test temperature is increased.

For the cubic 20Y material, such a plan is less likely to succeed, since it is impossible to orient a cubic crystal in such a way that every {111}<110> system is totally inaccessible. However, a near <111> axis would be fairly hard for this slip system.

The {001}<011> slip observed for 5Y-PSZ crystals is in agreement with the earlier work by McCartney, et al (8) on Ca-CSZ crystals compressed along the same axis at 1350C. What is surprising is the seemingly unusual {111} wavy slip experienced by 20-CSZ. However, it was noted by Hannink and Swain (6) that for yttria-stabilized cubic zirconia, hardness anisotropy was compatible with either {001}<011> or {111}<110>. That being the case, it is possible that for 20Y-CSZ, {111}<110> slip dominates for $T \lesssim 700C$, while the {001}<110> system is active at higher temperatures. In addition, it will be recalled that Michel, et al (3) observed cleavage on {111} for 16.2Y-CSZ crystals failed in bending, while Ingel (4) observed that the crystallographic dependence of K_{IC} for 20Y-CSZ exhibited a minimum along {111}. Actually, the waviness and "feathery" slip prevalent in 20Y-CSZ (Fig. 10) suggests that multiple slip systems are involved for $T \lesssim 700C$.

Recalling Fig. 5, it appears that $\sigma_c(T)$ for 5Y-PSZ may be composed of two branches with different slopes, the transition between these occurring around $300C < T < 500C$. It is possible that the lower temperature branch corresponds to {111}<110> slip, while the high temperature regime relates to flow on {001}<011>. Further TEM and X-ray slip trace analysis is in progress to test these possibilities.

The principal implication of the surface transformation observations is that they are not caused by tetragonal → monoclinic; rather, they probably are due to reversible (9) transformation (rhombohedral → cubic) of rhombohedral domains produced by polishing the cubic (20Y-CSZ) or cubic-tetragonal (5Y-PSZ) starting material. Since polishing marks were revealed during compression tests performed at temperatures as low as 250C, it is not likely that the transformations were thermal in origin. Raman spectroscopy showed no evidence of monoclinic phase on transformed surfaces, and Nomarski study of regions around diamond pyramid indentations in both CSZ and PSZ crystals showed absolutely no evidence of the characteristic cooperative shear bands created in such tests by tetragonal → monoclinic transformations (15).

These findings are in basic agreement with those of Hasegawa (9), regarding production of rhombohedral (r) material by the polishing of yttria-stabilized zirconia containing, or composed of, cubic phase. In his study, less r-phase was produced by polishing high Y (more cubic) material, which correlates with the present observation that only very intense polishing scratches in 20Y-CSZ seemed to transform under compression.

Based on these observations, it would appear that the strength and toughness of 5Y-PSZ and 20Y-CSZ single crystals have little or nothing to do with phase transformations. The tetragonal → monoclinic transformation does not occur in either tension (3,5) or compression, and the stress-assisted rhombohedral transformation probably is superficial and not capable of controlling bulk properties. The complex $K_C(T)$ behavior observed by Ingel, et al (2), must require an explanation based on

crystallographic orientation, microcleavage along certain planes, temperature-dependent plastic flow, and crack-precipitate interaction.

A simple view of such a concept is shown in Figure 14. At lower temperatures, crack growth resistance would be governed largely by crack-precipitate interactions, which result from lattice, elastic, and thermal expansion mismatches between the cubic matrix and its tetragonal precipitates. As the temperature rises, these contributions will decrease, probably faster than the increase in plasticity contribution, which will be orientation dependent as well. At elevated temperatures, plasticity will dominate, producing an apparent high toughness.

CONCLUSIONS

1. Compressive yield and ultimate strengths for 5Y-PSZ and 20Y-CSZ single crystals decrease rapidly with increasing temperature.
2. Plastic flow in 5Y-PSZ is planar on {100}, while slip in 20Y-CSZ is wavy on {111} and secondary systems.
3. Tetragonal → monoclinic transformations do not occur during compressive loading in either single crystal variant.
4. Compressive stresses appear to reverse cubic → rhombohedral transformations induced by polishing in both 5Y-PSZ and 20Y-CSZ.

Acknowledgements

The support of the Office of Naval Research under Contract No. N00014-84-C-0213 is gratefully acknowledged. Thanks is expressed to R. W. Rice for provision of the single crystals, and to T. W. Coyle who performed Raman spectroscopy of a deformed specimen.

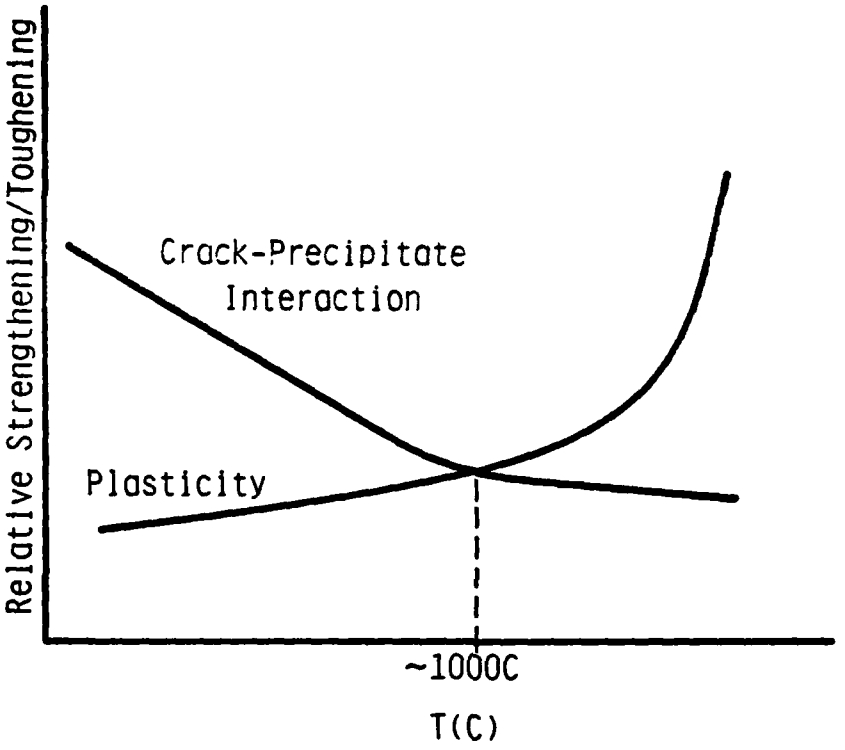

Figure 14. Conceptual model of temperature dependence of strengthening/toughening in Y-PSZ single crystal.

REFERENCES

1. R. P. Ingel, R. W. Rice, and D. Lewis, Com. Amer. Ceram. Soc. 65 (1982) C-108.
2. R. P. Ingel, D. Lewis, B. A. Bender, and R. W. Rice, Com. Amer. Ceram. Soc. 65 (1982) C-150.
3. D. Michel, L. Mazerolles, M. Perez Y Jorba, J. Mat. Sci. 18 (1983) 2618.
4. R. P. Ingel, "Structure-Mechanical Property Relationships for Single Crystal Yttrium Oxide Stabilized Zirconium Oxide", Ph.D. Dissertation, Catholic University of America (1982).
5. T. W. Coyle, "Transformation Toughening and the Martensitic Transformation in ZrO_2", Ph.D. Dissertation, Massachusetts Institute of Technology" (1985).
6. R. H. J. Hannink and M. V. Swain, Advances in Ceramics, Volume 12, Science and Technology of Zirconia, II, ed. N. Claussen, M. Ruhle, and A. H. Heuer, American Ceramic Society, Columbus (1985).
7. C. A. Brookes, J. B. O'Neil, and B. A. W. Redfern, Proc. Roy. Soc. A332 (1971) 73.
8. M. L. McCartney, W. T. Donlon, and A. H. Heuer, J. Mat. Sci. 15 (1980) 1063.
9. H. Hasegawa, J. Mat. Sci. Lttrs. 2 (1983) 91.
10. T. Sakuma, Y.-I. Hoshizawa, and H. Suto, J. Mat. Sci. Lttrs. 4 (1985) 29.
11. J. Lankford, J. Mat. Sci. 20 (1985) 53.

12. J. Lankford, J. Am. Cer. Soc. 64 (1981) C33.

13. J. Lankford, Fracture Mechanics of Ceramics, Vol. 5, Ed. R. C. Bradt, A. G. Evans, D. P. H. Hasselman, and F. F. Lange, Plenum Press, N.Y. (1983) 625.

14. J. Lankford, J. Am. Cer. Soc. 66 (1983) C212.

15. R. H. J. Hannink and M. V. Swain, J. Mat. Sci. 16 (1981) 1428.

END

FILMED

8-85

DTIC